A depth-averaged model for non-isothermal thin-film rimming flow

E.D. Kay [c], S. Hibberd [b], H. Power [a,*]

[a] Department of Mechanical, Materials and Manufacturing Engineering, University of Nottingham, Nottingham NG7 2RD, UK
[b] School of Mathematical Sciences, University of Nottingham, Nottingham NG7 2RD, UK
[c] Department of Mathematical Sciences, University of Nottingham Ningbo China, Ningbo 315100, China

Keywords:

Depth-averaged
Rimming flow
Non-isothermal
Thin-film

A B S T R A C T

A model for non-isothermal shear-driven thin-film flow on the inside surface of a stationary circular cylinder is presented. Motivated by an application to film flow in an aero-engine bearing chamber the model extends lubrication theory analysis of thin films to retain the important effects of inertia and heat convection.

The accuracy of the depth-averaged temperature model is tested and comparisons illustrate the model is accurate for both conduction- and convection-dominant flows although local inaccuracies are introduced in regions exhibiting sharp changes in boundary temperature when convective effects are strong.

Three rimming-flow configurations are considered: uni-directional flow with slowly-varying film height, a solution containing a steep front termed a shock, and a pooling solution where fluid accumulates in a recirculation at the base of the cylinder. The temperature field in the latter two which include recirculation features are greatly influenced by the strength of convection in the film.

1. Introduction

Modelling the temperature distribution in thin liquid films has a diverse range of applications. This study is motivated by the need to extend the modelling of shear-driven oil films in an aero-engine bearing chamber where heat transfer arises within highly-sheared thin films. Typical modelling of such films uses a lubrication approximation that neglects film inertia and heat convection which are important in this application.

In the context of an aero-engine bearing chamber thin liquid films develop on the walls of the chamber from oil used to lubricate provide a cooling mechanism. Such films are also subject to intense surface shear from nearby rotating shafts. Non-isothermal effects arise from temperature differences between the cylinder wall and the shearing airflow, or a temperature distribution around the cylinder wall may be developed from other nearby engine components. There is a vast literature on the dynamics of rimming flows, consult [1] for a review; these are generally considered with low Reynolds number which neglects the effect of film inertia. However for highly-sheared film flow these may be non-negligible as shown in [2] and correspondingly may significantly influence the heat-transfer.

In this paper we examine the non-isothermal flow of a thin liquid film on the inside of a partially-filled stationary cylinder driven by a constant surface shear. A depth-averaged approach to modelling the film is used as outlined in [2] and extended to include film temperature variation. The mass, momentum and energy conservation equations in the film are integrated through the depth of the film and incorporate the external boundary conditions through the upper and lower limits of integration. This approach is used to model open-channel flow [3,4] as it allows inertial effects and convection of heat to be retained as possible mechanisms at leading-order. Application of the approach to various instances of thin film flow has been by Gribben et al. [5]. The simplified approximations are obtained with the full flow field no-longer resolved precisely across the film but replaced by approximations for the velocity and temperature profiles through the film depth. A local quadratic profile is used for both film velocity and temperature. This approach is developed and the resulting film temperature field is verified by comparing against a fully resolved solution to a specimen case.

Temperature profiles in rimming and coating flows have been extensively studied using lubrication theory with inertia and heat convection typically negligible, for example [6], and good reviews of work on this is available in the recent publications [7,8]. Our paper aims to extend the thin film analysis by including these effects which may become important in the aero-engine application.

Additional relevant studies include non-isothermal planar thin film flows which we use as a test case and has characteristics shared with the rimming flow problem. An early paper on flow over an inclined uniformly-heated plane [9] employed a lubrication theory model to derive an evolution equation for film thickness, with evaporative and thermocapillary effects included, from which the stability of wave structures on the surface were studied.

* Corresponding author. Tel.: +44 01158466232; fax: +44 01159513800.
E-mail address: henry.power@nottingham.ac.uk (H. Power).

Nomenclature

α	lateral conduction parameter
ϕ_j	orthogonal functions
$\tau_a^*,\ \tau$	dimensional and dimensionless surface shear stress
Ai, Bi	Airy functions of first and second kind
c_j	Fourier coefficients
D	denominator in temperature profile coefficients
$f^0,\ f^1,\ Q^0,\ Q^1$	coefficients in integrated viscous and conduction terms
$I^0,\ I^1,\ J^0,\ J^1,\ K_h^0,\ K_q^0,\ K_h^1,\ K_q^1,\ W_0,\ Z_h^0,\ Z_q^0,\ M^0,\ M^1$	coefficients in inertia and convection integrals
k	thermal conductivity and smoothing parameter for wall temperature profile
L	half length of heated section of plate
$l_\theta,\ l_r$	azimuthal and radial components of surface unit tangent
$n_\theta,\ n_r$	azimuthal and radial components of surface unit normal
q	dimensionless film flux
r	radial coordinate
s	dimensionless circumferential coordinate
t	time
$T_w^*,\ T_w$	dimensional and dimensionless wall temperature
x	flat plate coordinate
y	dimensionless distance normal to wall
(u, v)	dimensionless velocity components
(u_r^*, u_θ^*)	dimensional velocity components in r and θ directions
$\bar{T}$	depth-averaged film temperature
B	surface Biot number
Ca	capillary number
ε	film aspect ratio
γ	surface heat transfer coefficient
κ	surface curvature
λ	gravity parameter and eigenvalues of Sturm–Liouville equation
μ	dynamic viscosity
Pe	film Péclet number
Re	film Reynolds number
ρ	density
Pe^*	reduced film Péclet number
Re^*	reduced film Reynolds number
σ	surface tension coefficient
θ	angular coordinate
A	filling fraction
$a_j^0,\ a_j^1$	leading and first order velocity profile coefficients
$b_j^0,\ b_j^1$	leading and first order temperature profile coefficients
g	acceleration due to gravity
$h^*,\ h$	dimensional and dimensionless film height
h_0	characteristic film height
$p^*,\ p$	dimensional and dimensionless film pressure
r_0	cylinder radius
$T^*,\ T$	dimensional and dimensionless film temperature
$T_a,\ T_b$	boundary temperatures on flat plate
U_0	characteristic film speed

This approach has subsequently been extended by various additions of, for example, inhomogeneities in substrate material [10], a surfactant-laden film surface [11] and, pertinent to this paper, local heating of the substrate [12,13]. Whilst representing a long-wavelength/lubrication theory approach similar to ours, these studies focus on the effect of temperature on the stability of surface structures but do not analyses the film temperature field that results which is the focus of our paper.

Local heating of planar films driven by an overlying air-shear have been extensively studied [14–17]. In [14] numerical simulations of the three-dimensional film flow field provided a detailed picture of the flow field in the film which was later compared to experimental data in [16]. We follow [15,17] in solution of the flat film temperature field via separation of variables and a Sturm–Liouville problem. Again we note from these that temperature effects are generally studied for their effect on surface structure stability though we note accord in results between our model and those of [17].

Common to many of papers e.g. [9–13,15] is the construction of an evolution equation for the film height containing terms that represent the temperature-related mechanisms. Importantly the film velocity and temperature field can be calculated once a solution of this evolution equation is obtained. Less well developed is use of a depth-averaged method for modelling non-isothermal thin films, in which a general form of the velocity and temperature field is specified a-priori. In [18] a study is presented covering locally heated planar flows with a parabolic velocity and linear temperature profiles resulting in a system of three coupled equations (continuity, momentum and energy). This is used to investigate free-surface stability. Nicol et al. [19] formulate a depth-averaged model for the dynamics and heat transfer in a thin film of condensate flowing on the cylindrical outer surface of a condenser and compare with experimental results.

A more common use of the depth-averaged approach is for larger-scale physical applications such as modelling lava flows [20] where a lubrication approximation is valid arising from the large disparity between the relevant horizontal and vertical length-scales. The depth-averaging method has been applied to thermal analyses of a smaller scale with the air cooling of printed circuit boards [21].

As a preliminary to studying rimming flow the depth-averaged model is applied to the case of uniform film flow over a horizontal plate with a locally heated patch. The existence of both an analytical [17] and numerical (using finite differences) solution for the two-dimensional temperature field for this specimen case provides a gauge against which to test the accuracy of the one-dimensional depth-averaged model.

The depth-averaged model is first applied to rimming flows of constant film height with imposed wall temperature profile providing localised heating. This is extended to a non-uniform film height profile with inhomogeneity in film temperature derived from a temperature difference between the walls and shearing airflow. Three characteristic rimming flows are examined in detail corresponding to the relative dominance of surface-shear over gravity forces. These are uniform, unidirectional film flow (strong shear), flow containing a recirculating pool at the base of the cylinder (weak shearing effect) and the intermediate case of the flow containing a recirculating shock feature. The dynamics of these three flow-types are complex depends on various physical parameters as elucidated in [22].

The structure of the paper is as follows. In Section 2 the depth-averaged model is formulated. In Section 3 the accuracy of the model is evaluated for the simplified case of a locally-heated planar film. Sections 4 and 5 examine uniform and non-uniform rimming flows and the effect convection and inertia on the temperature field. Conclusions are drawn in Section 6.

2. Model formulation

2.1. Film flow equations in cylindrical geometry

A liquid film completely coats the inner surface of a stationary cylinder of radius r_0 and is subject to a constant shear stress τ_a^* and pressure p_a^* at the surface. The liquid is taken to be incompressible and Newtonian with constant density ρ, dynamic viscosity μ, heat capacity c, thermal conductivity k. The flow field is taken as two-dimensional.

A cylindrical polar coordinate system (r, θ) is defined as shown in Fig. 1 where θ measures the angle from the vertically downward direction. Gravity $\mathbf{g} = g\cos\theta\hat{\mathbf{r}} - g\sin\theta\hat{\boldsymbol{\theta}}$ acts in the downward direction for a gravitational force per unit mass of g. The surface of the film has surface tension coefficient σ and is described by the surface $r^* = r^* - h^*(t^*, \theta)$. The film velocity, pressure and temperature fields are $\boldsymbol{u}^* = u_r^*\hat{\mathbf{r}} + u_\theta^*\hat{\boldsymbol{\theta}}, p^*$ and T^*. Here a superscript $*$ indicates dimensional variables and t^* represents time. The unit normal vector $\boldsymbol{n} = n_r\hat{\mathbf{r}} + n_\theta\hat{\boldsymbol{\theta}}$ and unit tangent vector $\boldsymbol{l} = l_r\hat{\mathbf{r}} + l_\theta\hat{\boldsymbol{\theta}}$ are given by

$$n_r = -N, \quad n_\theta = -\frac{N}{H}\frac{\partial h^*}{\partial\theta}, \quad l_r = -\frac{N}{H}\frac{\partial h^*}{\partial\theta}, \quad l_\theta = N, \tag{1}$$

where

$$N = N(\theta, t^*) = \left(1 + \left(\frac{1}{H^*}\frac{\partial h^*}{\partial\theta}\right)^2\right)^{-1/2} \tag{2}$$

and $H^* = H^*(\theta, t^*) = r_0 - h^*(\theta, t^*)$. The curvature of the interface κ^* is calculated from the divergence of the normal vector on the interface:

$$\kappa^* = \nabla^*\cdot\boldsymbol{n} \quad \text{on} \quad r^* = r_0 - h^*. \tag{3}$$

Conservation of energy in the film and the Navier–Stokes equations are

$$\rho c D^*T^*/Dt^* = k\nabla^{*2}T^*, \tag{4}$$

$$\nabla^*\cdot\boldsymbol{u}^* = 0, \tag{5}$$

$$\rho D^*\boldsymbol{u}^*/Dt^* = -\nabla^*p^* + \rho\boldsymbol{g} + \mu\nabla^{*2}\boldsymbol{u}^*. \tag{6}$$

In the above ∇^* is the dimensional gradient and $D^*/Dt^* = \partial/\partial t^* + \boldsymbol{u}^*\cdot\nabla^*$ is the dimensional convected derivative. The boundary conditions on the cylinder walls are the no-slip and no-penetration conditions on the film velocity together with a prescribed temperature T_w^* on the wall, i.e.,

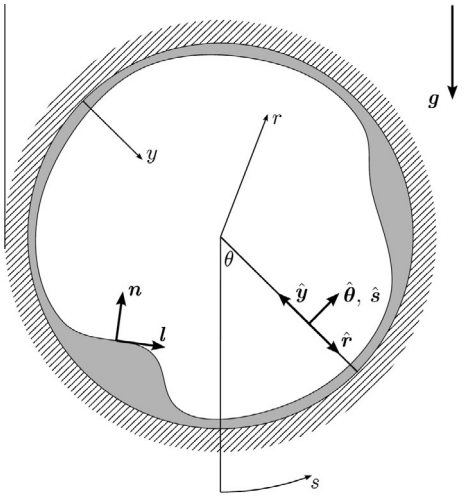

Fig. 1. Cylinder geometry and coordinate system.

$$\boldsymbol{u}^* = 0 \quad \text{and} \quad T^* = T_w^* \quad \text{on} \quad r^* = r_0. \tag{7}$$

Across the film surface at $r^* = r_0 - h^*$ the heat flux is proportional to the temperature difference across the interface by γ a heat transfer coefficient, there is a jump in the stress tensor $\boldsymbol{S}^*$ due to surface tension and a kinematic equation prescribes the evolution of the interface

$$\gamma(T_a^* - T^*) = k\nabla^*T^*\cdot\boldsymbol{n}, \tag{8}$$

$$\boldsymbol{n}\boldsymbol{S}^* = -p_a^*\boldsymbol{n} - \sigma\kappa^*\boldsymbol{n} + \tau_a^*\boldsymbol{l}, \tag{9}$$

$$\frac{\partial H^*}{\partial t^*} + \boldsymbol{u}\cdot\nabla^*H^* = 0. \tag{10}$$

To evaluate the leading-order thermal and dynamic behaviour the following non-dimensional variables and physical quantities are introduced

$$\begin{aligned} &t^* = r_0 t/U_0, \quad \kappa^* = \kappa/r_0, \\ &(u_\theta^*, u_r^*) = U_0(u, -\varepsilon v), \quad p^* = \rho U_0^2 p, \\ &\tau_a^* = \tau\mu U_0/h_0, \quad T^* = T_w^*T, \quad h^* = h_0 h. \end{aligned} \tag{11}$$

For a thin film the aspect ratio ε is small ($\varepsilon \ll 1$). In (11) U_0 is a typical film speed, h_0 a typical film height and the surface shear stress τ_a^* has been scaled by viscosity. Coordinates $s = \theta$ and $y = (r_0 - r^*)/h_0$ are the local film coordinates as shown in Fig. 1. These scalings give rise to the non-dimensional parameters

$$\begin{aligned} &\varepsilon = h_0/r_0, \quad \mathrm{Re} = \rho U_0 h_0/\mu, \quad \mathrm{Pe} = \rho c U_0 h_0/k, \\ &\mathrm{Ca} = \mu U_0/\sigma, \quad \lambda = \rho g h_0^2/\mu U_0, \quad \mathrm{B} = h_0\gamma/k. \end{aligned} \tag{12}$$

These are respectively the film aspect ratio, the Reynolds number, Péclet number, Capillary number, a ratio of gravitational to viscous forces and the interface Biot number. The dynamic pressure ρU_0^2 is selected to ensure azimuthal pressure gradients are retained (see Section 2.2) as this has been identified previously as an important stabilizing mechanism [22].

In the non-dimensional coordinate system the energy equation (4) is

$$\varepsilon\mathrm{Pe}\left(\frac{\partial T}{\partial t} + v\frac{\partial T}{\partial y} + \frac{u}{1-\varepsilon y}\frac{\partial T}{\partial s}\right) = \frac{\partial^2 T}{\partial y^2} - \frac{\varepsilon}{1-\varepsilon y}\frac{\partial T}{\partial y} + \frac{\varepsilon^2}{(1-\varepsilon y)^2}\frac{\partial^2 T}{\partial s^2}. \tag{13}$$

The wall boundary condition (7) is

$$u = v = 0 \quad \text{and} \quad T = T_w \quad \text{on} \quad y = 0 \tag{14}$$

and the interface conditions (8) and (10) give, on $y = h$,

$$\mathrm{B}(T_a - T)N^{-1} = \frac{\partial T}{\partial y} - \frac{\varepsilon^2 h'}{H^2}\frac{\partial T}{\partial s}, \tag{15}$$

$$\frac{\partial h}{\partial t} + \frac{\varepsilon h'}{H}u - v = 0, \tag{16}$$

where $H(s,t) = 1 - \varepsilon h(s,t)$ and $N = (1 + (\varepsilon h'/H)^2)^{-1/2}$ in dimensionless variables. Dimensionless forms of the continuity equation (5), and normal and tangential components of the momentum Eq. (6) and surface boundary condition (9) are respectively

$$\frac{\partial v}{\partial y} + \frac{1}{1-\varepsilon y}\frac{\partial u}{\partial s} - \frac{\varepsilon v}{1-\varepsilon y} = 0, \tag{17}$$

$$\begin{aligned} \varepsilon\mathrm{Re}\left(\varepsilon\frac{\partial v}{\partial t} + \varepsilon v\frac{\partial v}{\partial y} + \frac{\varepsilon u}{1-\varepsilon y}\frac{\partial v}{\partial s} + \frac{u^2}{1-\varepsilon y}\right) &= -\mathrm{Re}\,\frac{\partial p}{\partial y} - \lambda\cos s \\ &+ \varepsilon\frac{\partial^2 v}{\partial y^2} - \frac{\varepsilon^2}{1-\varepsilon y}\frac{\partial v}{\partial y} - \frac{\varepsilon^3}{(1-\varepsilon y)^2}\frac{\partial^2 v}{\partial s^2} - \frac{\varepsilon^3 v}{(1-\varepsilon y)^2} \\ &+ \frac{2\varepsilon^2}{(1-\varepsilon y)^2}\frac{\partial u}{\partial s}, \end{aligned} \tag{18}$$

$$\varepsilon\mathrm{Re}\left(\frac{\partial u}{\partial t}+v\frac{\partial u}{\partial y}+\frac{u}{1-\varepsilon y}\frac{\partial u}{\partial s}-\frac{\varepsilon u v}{1-\varepsilon y}\right)=-\frac{\varepsilon\mathrm{Re}}{1-\varepsilon y}\frac{\partial p}{\partial s}-\lambda\sin s+\frac{\partial^2 u}{\partial y^2}-\frac{\varepsilon}{1-\varepsilon y}\frac{\partial u}{\partial y}+\frac{\varepsilon^2}{1-\varepsilon y}\frac{\partial^2 u}{\partial s^2}-\frac{2\varepsilon^3}{(1-\varepsilon y)^2}\frac{\partial v}{\partial s}-\frac{\varepsilon^2 u}{(1-\varepsilon y)^2},\quad(19)$$

$$p_a=-\frac{2N^2}{\mathrm{Re}}\left\{\varepsilon\frac{\partial v}{\partial y}-\left(\frac{\partial u}{\partial y}+\frac{\varepsilon u}{H}+\frac{\varepsilon^2}{H}\frac{\partial v}{\partial s}\right)\frac{\varepsilon h'}{H}+\left(\frac{\varepsilon}{H}\frac{\partial u}{\partial s}-\frac{\varepsilon^2 v}{H}\right)\left(\frac{\varepsilon h'}{H}\right)\right\}+p-\frac{\varepsilon\kappa}{\mathrm{ReCa}},\quad(20)$$

$$\tau N^{-2}=\left(1-\left(\frac{\varepsilon h'}{H}\right)^2\right)\left(\frac{\partial u}{\partial y}+\frac{\varepsilon u}{H}+\frac{\varepsilon^2}{H}\frac{\partial v}{\partial s}\right)+2\frac{\varepsilon h'}{H}\left(\varepsilon^2\frac{\partial v}{\partial y}-\frac{\varepsilon^2}{H}\frac{\partial u}{\partial s}+\frac{\varepsilon^2 v}{H}\right).\quad(21)$$

The film surface curvature (3) is

$$\kappa=\frac{N}{H}\left[\left(\frac{\varepsilon h''}{H}+\left(\frac{\varepsilon h'}{H}\right)^2\right)\left(\left(\frac{\varepsilon N h'}{H}\right)^2-1\right)-1\right].\quad(22)$$

2.2. Thin film equations with inertial effects

In an aero-engine bearing chamber or other applications involving high surface shear, thin films may experience moderate inertial and heat-convection effects corresponding to $\varepsilon\mathrm{Re}\sim O(1)$ and $\varepsilon\mathrm{Pe}\sim O(1)$ respectively, i.e. inertia and convection as leading-order effects. The model developed in this paper is thereafter formulated accurate to $O(\varepsilon)$ for dimensionless parameters within the moderate inertia and convection regime

$$\varepsilon\ll 1,\quad \mathrm{Re}\sim O(1/\varepsilon),\quad \mathrm{Pe}\sim O(1/\varepsilon)\quad\text{and}\quad \lambda\sim O(1).\quad(23)$$

The relation with λ in (23) includes the classical lubrication theory limit $\varepsilon\ll 1$ which yields a constant pressure through the film; we note after [23] that this is insufficient to model the abrupt changes in pressure in the pool solution due to hydrostatic effects in regions of high film height gradient. To include such effects gravity terms of $O(\varepsilon)$ must be included and our model is made accurate to $O(\varepsilon)$. Hydrostatic terms are multiplied by h' which allows these effects to be locally promoted to leading order in regions of sharp film height variation. Similarly we include a lateral diffusion term from (13), despite its appearance at $O(\varepsilon^2)$, as this may become significant in regions of high temperature gradient. With ε and Pe satisfying (23) the energy equation (13) can be written

$$\varepsilon\mathrm{Pe}\left(\frac{\partial T}{\partial t}+u\frac{\partial T}{\partial s}+v\frac{\partial T}{\partial y}+\varepsilon y u\frac{\partial T}{\partial s}\right)=\frac{\partial^2 T}{\partial y^2}-\varepsilon\frac{\partial T}{\partial y}+\varepsilon^2\frac{\partial^2 T}{\partial s^2}+O(\varepsilon^2,\varepsilon^3\mathrm{Pe})\quad(24)$$

The wall boundary condition remains as (14); interface heat flux (15) and kinematic conditions (16) on $y=h$ become

$$\mathrm{B}(T_a-T)=\frac{\partial T}{\partial y}+O(\varepsilon^2),\quad(25)$$

$$\frac{\partial h}{\partial t}+u\frac{\partial h}{\partial s}+\varepsilon h u\frac{\partial h}{\partial s}-v=O(\varepsilon^2).\quad(26)$$

To $O(\varepsilon)$ the governing Eqs. (17)–(19) and boundary conditions (20) and (21) for film dynamics are

$$(1-\varepsilon y)\frac{\partial v}{\partial y}+\frac{\partial u}{\partial s}-\varepsilon v=0,\quad(27)$$

$$\varepsilon^2\mathrm{Re}u^2=-\varepsilon\mathrm{Re}\frac{\partial p}{\partial y}-\varepsilon\lambda\cos(s)+O(\varepsilon^2,\varepsilon^3\mathrm{Re}),\quad(28)$$

$$\varepsilon\mathrm{Re}\left(\frac{\partial u}{\partial t}+v\frac{\partial u}{\partial y}+u\frac{\partial u}{\partial s}+\varepsilon y u\frac{\partial u}{\partial s}-\varepsilon u v\right)=-\varepsilon\mathrm{Re}\frac{\partial p}{\partial s}-\lambda\sin(s)+\frac{\partial^2 u}{\partial y^2}-\varepsilon\frac{\partial u}{\partial y}+O(\varepsilon^2,\varepsilon^3\mathrm{Re}),\quad(29)$$

$$p_a=p-\frac{\varepsilon\kappa}{\mathrm{ReCa}}+O(\varepsilon),\quad(30)$$

$$\tau=\frac{\partial u}{\partial y}+\varepsilon u+O(\varepsilon^2)\quad(31)$$

and the curvature (22) is approximated by $\kappa=1-\varepsilon(h+h'')$.

2.3. Depth-averaging

Following [2] the energy equation (24) is reduced to a spatially one-dimensional problem and boundary conditions (14), (25) and (26) incorporated by first applying a depth-averaging procedure to evaluate a mean film temperature. Similar expressions are obtained for film dynamics by depth-averaging the continuity (27) and azimuthal momentum (29) equations. The system is solved for a film height profile h, film volume flux q and depth-averaged film temperature $\bar{T}$ given by

$$q=\int_0^h u\,dy,\quad \bar{T}=\frac{1}{h}\int_0^h T\,dy.\quad(32)$$

The depth-averaged azimuthal film velocity is defined by $\bar{u}=q/h$. Reconstruction of the film flow fields can be approximated from these variables as described later. This integral method is used by Nguyen and Balakotaiah [24] for planar film dynamics and, with a linear temperature profile, by Kalliadasis et al. [18] for locally-heated planar flows.

The depth-averaged energy equation (24) is

$$\varepsilon\mathrm{Pe}\left[\frac{\partial}{\partial t}\int_0^h T\,dy+\frac{\partial}{\partial s}\int_0^h uT\,dy+\varepsilon\frac{\partial}{\partial s}\int_0^h yuT\,dy-\varepsilon\int_0^h vT dy\right]=\left[\frac{\partial T}{\partial y}-\varepsilon T\right]_0^h+\varepsilon^2\left(\frac{\partial^2}{\partial s^2}\int_0^h T\,dy-2\frac{\partial T|_h}{\partial s}-T|_h h''\right)+O(\varepsilon^2).\quad(33)$$

with notation $[a]_0^h=a(y=h)-a(y=0)$. From [2] the depth-averaged continuity (27) and momentum (29) equations are

$$(1-\varepsilon h)\frac{\partial h}{\partial t}+\frac{\partial q}{\partial s}=O(\varepsilon^2),\quad(34)$$

$$\varepsilon\mathrm{Re}\left[\frac{\partial}{\partial t}\int_0^h u\,dy+\frac{\partial}{\partial s}\int_0^h u^2\,dy+\varepsilon\frac{\partial}{\partial s}\int_0^h yu^2\,dy-2\varepsilon\int_0^h uv dy\right]=-\lambda h\sin s+\frac{\varepsilon^3}{\mathrm{Ca}}h(h'+h''')-\varepsilon^2\mathrm{Re}\frac{\partial}{\partial s}\int_0^h\left(\int_0^h u^2 dy-\int_0^y u^2 dy\right)dy-\varepsilon\lambda\frac{\partial}{\partial s}\left(\frac{h^2\cos s}{2}\right)+\left[\frac{\partial u}{\partial y}-\varepsilon u\right]_0^h+O(\varepsilon^2,\varepsilon^3\mathrm{Re}).\quad(35)$$

The surface tension terms which appear at $O(\varepsilon^3)$ in (35) are retained as these are known to become important in regions where h''' is large due to sharp changes in film height.

It is convenient to introduce the reduced Péclet and Reynolds numbers $\mathrm{Pe}^*=\varepsilon\mathrm{Pe}$ and $\mathrm{Re}^*=\varepsilon\mathrm{Re}$ giving the size of the convection and inertia terms in (33) and (35) respectively. The regime of the model (23) is for $\mathrm{Re}^*\sim O(1)$ and $\mathrm{Pe}^*\sim O(1)$.

2.4. Thin film velocity and temperature profiles

Evaluation of the integral terms in (33) and (35) is obtained by prescribing a local functional form for the velocity and temperature across the film and globally with corresponding coefficients which vary with azimuthal position around the cylinder. Quadratic velocity and temperature profiles across the film are prescribed of the form

$$\begin{aligned} &u = u^0 + \varepsilon u^1, \quad T = T^0 + \varepsilon T^1, \\ &u^0 = a_1^0 y + a_2^0 y^2, \quad u^1 = a_1^1 y + a_2^1 y^2, \\ &T^0 = b_0^0 + b_1^0 y + b_2^0 y^2, \quad T^1 = b_0^1 + b_1^1 y + b_2^1 y^2. \end{aligned} \tag{36}$$

The velocity profile automatically satisfy the no-slip condition (14) and reduces to an exact representation in the case of Stokes flow. In (36) the leading- and first-order coefficients $a_i = a_i(s,t)$ and $b_i = b_i(s,t)$ (identified by a superscript 0 and 1 respectively) are determined in terms of h, q and $\bar{T}$ by applying the surface and wall boundary conditions and integral conditions (32).

For the temperature profile, (14) gives leading-order and $O(\varepsilon)$ components $b_0^0 = T_w$ and $b_0^1 = 0$ respectively. The surface (25) and integral (32) conditions give at leading-order

$$\begin{aligned} &b_1^0 h/2 + b_2^0 h^2/3 = \bar{T} - T_w, \\ &b_1^0(1 + Bh) + b_2^0(2h + Bh^2) = B(T_a - T_w) \end{aligned} \tag{37}$$

and at $O(\varepsilon)$

$$\begin{aligned} &b_1^1/2 + b_2^1 h/3 = 0, \\ &(1 + Bh) b_1^1 + (2h + Bh^2) b_2^1 = 0. \end{aligned} \tag{38}$$

The $O(\varepsilon)$ system has the trivial solution $b_1^1 = b_2^1 = 0$ and the leading-order system has solution

$$\begin{aligned} b_1 &= (-12T_w - 4h\mathrm{B}T_w - 2h\mathrm{B}T_a + 12\bar{T} + 6\mathrm{B}h\bar{T})/Dh, \\ b_2 &= (6T_w + 3h\mathrm{B}T_a + 3h\mathrm{B}T_w - 6\bar{T} - 6\mathrm{B}h\bar{T})/Dh^2 \end{aligned} \tag{39}$$

with $D = 4 + \mathrm{B}h$.

Following the same approach for the velocity profile, wall (14) and surface (31) boundary conditions along with the integral condition (32) on the film flux allow calculation of a_j^0 and a_j^1 as

$$\begin{aligned} &a_1^0 = -\tau/2 + 3q/h^2, \quad a_2^0 = 3\tau/4h - 3q/2h^3, \\ &a_1^1 = 3q/4h + h\tau/8, \quad a_2^1 = -9q/8h^2 - 3\tau/16. \end{aligned} \tag{40}$$

The radial velocity profile, required in calculation of the second $O(\varepsilon)$ integral in (35), is

$$v^0 = -\left(\frac{\partial a_1^0}{\partial h} h' + \frac{\partial a_1^0}{\partial q} q'\right)\frac{y^2}{2} - \left(\frac{\partial a_2^0}{\partial h} h' + \frac{\partial a_2^0}{\partial q} q'\right)\frac{y^3}{3}. \tag{41}$$

We direct the reader to [2] for details.

All coefficients in (36) are now given in terms of h, q and $\bar{T}$. Variations in h, q and $\bar{T}$ around the cylinder are given from solving (33)–(35). Relevant integral terms can now be found as follows

$$\begin{aligned} &\int_0^h u^2 dy = \int_0^h (u^0)^2 + 2\varepsilon \int_0^h u^0 u^1 dy = I^0 + \varepsilon I^1, \\ &\int yu^2 dy = \int_0^h \left(\int_0^h u^2 dy - \int_0^y u^2 dy\right) dy = \int y(u^0)^2 dy = J^0, \\ &\int_0^h u v dy = \int_0^h u^0 v^0 dy = K_h^0 h' + K_q^0 q', \\ &\int_0^h uT dy = \int_0^h u^0 T^0 dy + \varepsilon \int_0^h u^1 T^0 dy = M^0 + \varepsilon M^1, \\ &\int_0^h yuT dy = \int_0^h yu^0 T^0 dy = W^0, \\ &\int_0^h vT dy = \int_0^h v^0 T^0 dy = Z_h^0 h' + Z_q^0 q'. \end{aligned} \tag{42}$$

Further,

$$\left[\frac{\partial u}{\partial y} - \varepsilon u\right]_0^h = f^0 + \varepsilon f^1, \quad \left[\frac{\partial T}{\partial y} - \varepsilon T\right]_0^h = Q^0 + \varepsilon Q^1. \tag{43}$$

Coefficient functions in (42) and (43) are given in Appendix A.

The resulting system of three coupled Eqs. (33)–(35) represents the final depth-averaged model for non-isothermal film flow and is solved to give profiles for $h(s,t)$, $q(s,t)$ and $\bar{T}(s,t)$. Rimming flows correspond to periodic solutions for $h(s,t)$, $q(s,t)$ and $\bar{T}(s,t)$ in $-\pi \leqslant s \leqslant \pi$, i.e.,

$$h(-\pi) = h(\pi), \quad q(-\pi) = q(\pi) \quad \text{and} \quad \bar{T}(-\pi) = \bar{T}(\pi). \tag{44}$$

3. Uniform flow over a heated plate

In this section the accuracy of the depth-averaged approach is tested in the case of shear-driven uniform film flow over a flat plate with a heated patch. Here the Navier–Stokes equations have an exact solution corresponding to shear flow with a linear velocity profile. In the case of Dirichlet temperature boundary conditions, solutions of the corresponding two-dimensional energy equation are found analytical following [17] and numerically using finite-differences and are used to examine the capacity of the depth-averaged temperature model to provide a reconstructed film temperature field.

For this section $x^* = Lx$ denotes distance along the plate containing a heated patch of length $2L$. The velocity field in a uniform flow of constant film height h_0 driven across a plate by an imposed surface shear stress τ_a^* has an exact solution $(u^*, v^*) = (\tau_a^* y^*/\mu, 0)$. With $U_0 = \tau_a^* h_0/\mu$ the dimensionless velocity field is classical shear flow $(u, v) = (y, 0)$ with $\mathrm{Re} = \rho h_0^2 \tau_a^*/\mu^2$, $\mathrm{Pe} = \tau_a^* h_0^2/\mu\kappa$, $\tau = 1$ and dimensionless flux $q = 1/2$. The uniform film ($h = 1$) now occupies the domain $0 \leqslant y \leqslant 1$ and $-\infty \leqslant x \leqslant \infty$.

A wall temperature profile

$$T_w(x) = \begin{cases} \frac{1}{2}(T_a - T_b)[1 - \tanh(+k[x + L])] + T_b, & x \leqslant 0, \\ \frac{1}{2}(T_a - T_b)[1 - \tanh(-k[x - L])] + T_b, & x > 0 \end{cases} \tag{45}$$

is specified corresponding to a uniformly heated wall of temperature T_a with a region $-L < x < L$ heated to temperature T_b. Narrow regions around $x = \pm L$ smoothly link the localised inner temperature T_b with an asymptotic far field temperature T_a. The parameter $k > 0$ controls the width of the transition region and as $k \to \infty$ the profile tends to a step function.

Under shear flow the two-dimensional film temperature field is governed by the convection–diffusion equation

$$\mathrm{Pe}^* y \frac{\partial T}{\partial x} = \frac{\partial^2 T}{\partial y^2} + \alpha \frac{\partial^2 T}{\partial x^2} \quad \text{in} \quad 0 \leqslant y \leqslant 1, \ -\infty \leqslant x \leqslant \infty, \tag{46}$$

where $\alpha = \varepsilon^2$ and $\varepsilon = h_0/L$. In this case of planar flow (46) is exact for arbitrary Pe^* as compared to the rimming-flow analogue (24) which is restricted up to $\mathrm{Pe}^* \sim O(1)$. Eq. (46) possesses an analytical solution in the case of the Dirichlet surface and wall boundary conditions

$$\begin{aligned} &T = T_b \quad \text{on} \quad y = 1, \\ &T = T_w(x) \quad \text{on} \quad y = 0 \end{aligned} \tag{47}$$

with far field condition $T(x = \pm\infty, y) = T_a$.

Following Section 2, a quadratic temperature profile (36) is selected which satisfies both (47) and the definition of mean temperature from (32). Substituting into (46) gives a one-dimensional equation which governs the depth-averaged film temperature,

$$\mathrm{Pe}^*\left(\frac{1}{2}\frac{\mathrm{d}\bar{T}}{\mathrm{d}x} - \frac{1}{12}\frac{\mathrm{d}T_w}{\mathrm{d}x}\right) = 6(T_a + T_w - 2\bar{T}) + \alpha\frac{\mathrm{d}^2\bar{T}}{\mathrm{d}x^2}. \tag{48}$$

Eq. (48) is the analogue of (33) for flow over a heated patch and the mean film temperature must satisfy the far field conditions $\bar{T}(x=\pm\infty)=T_a$.

The remainder of this section tests the accuracy of solutions obtained from the simpler depth-averaged temperature Eq. (48) against those of the two-dimensional temperature Eq. (46) obtained both analytically and numerically.

3.1. Analytical and numerical solutions to two-dimensional temperature field

The case $\alpha=0$ corresponds to negligible lateral conduction with a balance between conduction in the vertical direction and convection in the horizontal direction. A separable solution for the film temperature in the case $k\to\infty$, representing a discrete heated patch, is found following [17] in each region. The solution is

$$T(x,y)=T_a \quad \text{in} \quad x\leqslant -L, \tag{49}$$

$$T(x,y)=\sum_{j=1}^{\infty} c_{2j}\phi_{2j}e^{-\lambda_j(x+L)/\mathrm{Pe}^*}+(T_a-T_b)y+T_b \quad \text{in} \quad |x|<L, \tag{50}$$

$$T(x,y)=\sum_{j=1}^{\infty} c_{3j}\phi_{3j}e^{-\lambda_j(x+L)/\mathrm{Pe}^*}+T_a \quad \text{in} \quad x>L \tag{51}$$

corresponding to the regions upstream, above and downstream of the plate respectively. The set of eigenvalues λ_j satisfy $\sqrt{3}\mathrm{Ai}(-\lambda_j^{1/3})-\mathrm{Bi}(-\lambda_j^{1/3})=0$ and eigenfunctions $\phi_j=\sqrt{3}\mathrm{Ai}(-\lambda_j^{1/3}y)-\mathrm{Bi}(-\lambda_j^{1/3}y)$. ϕ_{2j} indicates the set of ϕ_j in the region above the patch $(-L<x\leqslant L)$, ϕ_{3j} in the region downstream of the patch $(x>L)$. The orthogonality of ϕ_j allows the coefficients c_{2j} and c_{3j} to be calculated as

$$c_{2j}=\frac{\int_0^1 y\,\phi_{2j}(y)[(T_a-T_b)(1-y)]dy}{\int_0^1 y\,\phi_{2j}^2(y)dy}, \tag{52}$$

$$c_{3j}=\frac{\int_0^1 y\,\phi_{3j}(y)f_3(y)e^{2\lambda_j L/\mathrm{Pe}^*}dy}{\int_0^1 y\,\phi_{3j}^2(y)dy}. \tag{53}$$

Using (53), $f_3(y)$ is given by

$$\sum_{j=1}^{\infty} c_{2j}\phi_{2j}e^{-2\lambda_j L/\mathrm{Pe}^*}=T_2(L,y)-T_a\equiv f_3(y), \tag{54}$$

where $T_2(L,y)$ is the temperature field on the downstream end of the patch and is a given from the coefficients c_{2j}.

The general solution for (46) with $\alpha\neq 0$ must be found numerically. A finite difference scheme is applied to a rectangular grid of points which in each direction are uniformly-spaced. Second-order central differences approximate second-order derivatives and third-order upwinding is used to approximate the convective $\mathrm{Pe}^* y\partial T/\partial x$ term. The resulting set of coupled non-linear algebraic equations are solved in Matlab using the in-built `fsolve` function to give the approximated temperature at each grid point.

A comparison of the mean film temperatures from the exact solution (49)–(51) and the two-dimensional finite difference (2DFD) solution for three values of Pe^* is shown in Fig. 2. It was found sufficient to include the first 25 terms in the infinite sums in (50) and (51). Including further terms was found to change the average film temperature by less than 10^{-8}. Agreement between the two methods is shown in Fig. 2 for increasing Pe^* indicating that the convection term is well approximated in the 2DFD scheme. Around the ends of the patch $(x=\pm 1)$ T_w is discontinuous and there is a numerical error in the 2DFD solution expected in the absence of smoothing from lateral conduction.

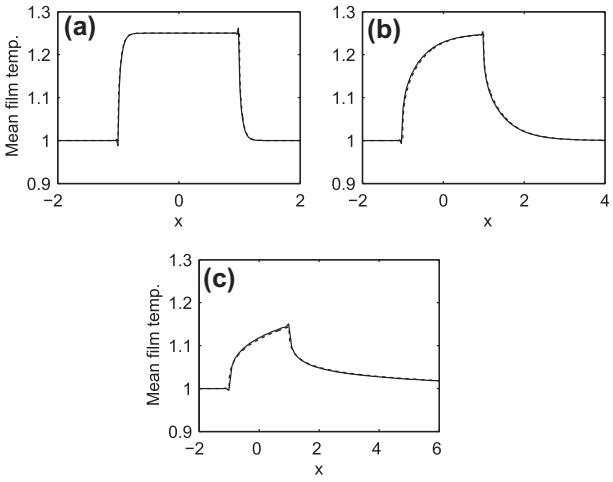

Fig. 2. Comparison of mean film temperature from analytic (· · · · · ·) and 2D finite differences (—) solutions to (46) ($\alpha=0$). (a) $\mathrm{Pe}^*=1$, (b) $\mathrm{Pe}^*=10$ and (c) $\mathrm{Pe}^*=100$.

Fig. 2 shows this error does not depend on Pe^* and so is indicative this is not a problem related to convection.

In this section the analytic solution (49)–(51) has provided a measure of the accuracy of the numerical 2DFD solution. In the following section the 2DFD solution method will be used to evaluate the accuracy of the depth-averaged (DA) approach.

3.2. Comparison of depth-averaged method with full two-dimensional solution

The depth-averaged method is applied to the test case with the (48) solved numerically for $\bar{T}(x)$; the film temperature $T(x,y)$ is reconstructed from the definition of the quadratic temperature profile (36). The numerical scheme is that described in Section 3.1 with discretisation in only one spatial direction. Using the 2DFD numerical solution as a reference the accuracy of the depth-averaged formulation is tested. The 2DFD temperature field $T(x,y)$ is also retrospectively depth-averaged to obtain $\bar{T}(x)$ to compare with the solution of (48). The lateral conduction mechanism is included.

A first comparison is of mean temperature profiles. Results illustrated in Fig. 3 for flow over a smoothed wall temperature $(k=1)$ with $\mathrm{Pe}^*=1, 10$ and 100 show good agreement between the two approaches for both conduction- and convection-dominant flows. The heated region extends further downstream with increasing convection: for $\mathrm{Pe}^*=1$, case (a), $\bar{T}$ follows the wall temperature and for $\mathrm{Pe}^*=100$, case (c), $\bar{T}$ returns to T_a within approximately one patch length.

Comparisons of $T(x,y)$ and a series of calculated profiles through the depth of the film are shown in Fig. 4 for $\mathrm{Pe}^*=100$. Results show good agreement indicating the full temperature field may be accurately reconstructed from a mean temperature profile. Any discrepancy is in regions where T_w changes rapidly; at the midpoint of the heated section the temperature contours are coincident. In case (d) the profile from the 2DFD solution in the region $y>0.5$ is nearly constant and cannot be replicated by the quadratic profile (36). This produces an underestimation of the film temperature. Temperature contours and profiles of the low convection case $\mathrm{Pe}^*=1$ give excellent agreement over the domain as profiles are linear (the exact solution to the conduction-dominant case).

The analysis is repeated with $k=100$ – the case of a sharp change in wall temperature around $x=\pm L$. Comparison of mean temperature from the two methods is shown in Fig. 5. The depth-averaged solution is in very good agreement with the 2DFD solution

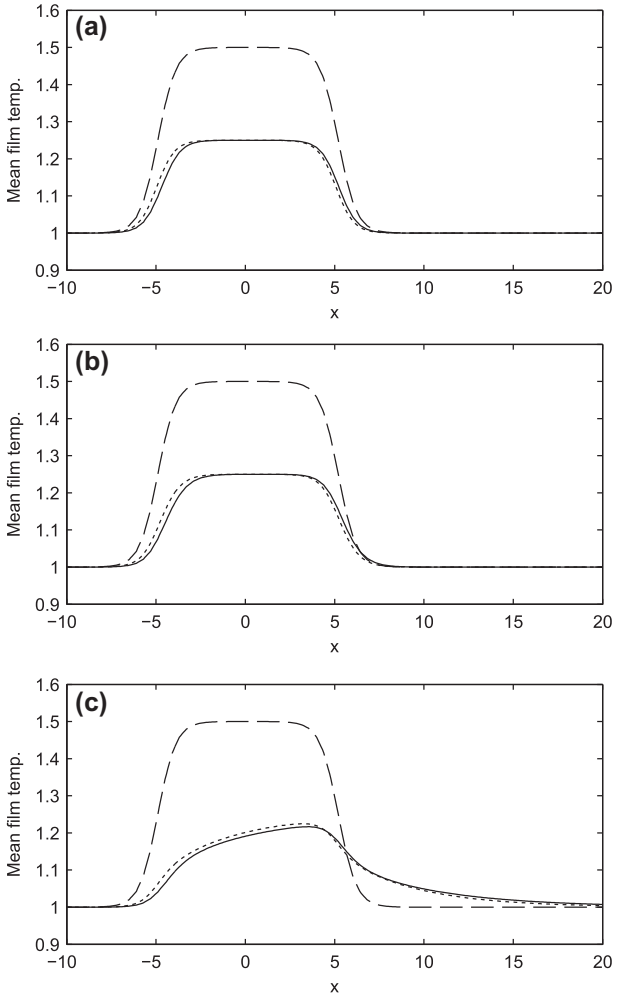

Fig. 3. Mean film temperature for the depth-averaged (·····) and 2DFD (—) methods. Wall temperature profile T_w indicated by (- - -). (a) $\mathrm{Pe}^* = 1$, (b) $\mathrm{Pe}^* = 10$ and (c) $\mathrm{Pe}^* = 100$. $T_a = 1,\ T_b = 1.5,\ \varepsilon = 0.1,\ L = 5,\ k = 1$.

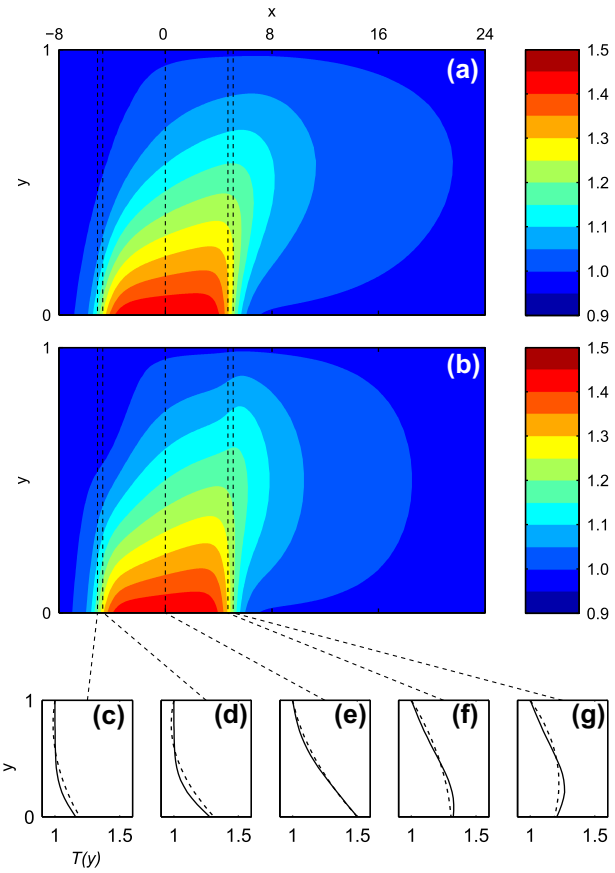

Fig. 4. Film temperature fields for $\mathrm{Pe}^* = 100$ with $k = 1$ using (a) 2DFD and (b) DA solution methods. (c)–(g) show temperature profiles through the film at points indicated by connecting lines; 2DFD solution (—) and depth-averaged solution (- - -). Other parameters as in Fig. 3.

across the range of Pe^* values and even in the convection-dominant case with $\mathrm{Pe}^* = 100$ (c) there is only a slight over- and under-estimation of $\bar{T}$ at the upstream and downstream ends of the heated section respectively. Convective effects extend the heated region downstream and $\bar{T}$ returns to the far-field temperature over a similar distance as for $k = 1$. When $T(x,y)$ is reconstructed from $\bar{T}(x)$ cases $\mathrm{Pe}^* = 1$ and $\mathrm{Pe}^* = 10$ give excellent agreement and are not shown. Results for $\mathrm{Pe}^* = 100$ are shown in Fig. 6.

An inaccuracy in $\bar{T}$ at the ends of the plate is more apparent in the reconstructed field. This arises because the local temperature field (2DFD) changes sharply in response to the sharp change in wall temperature producing a distribution not well-modelled locally by a quadratic profile; as previously the constant temperature region in (d) cannot be accurately fitted by the quadratic. The film temperature obtained from the depth-averaged method is particularly accurate in regions where T_w does not change too rapidly (cases (e) and (f)) but inaccuracies are introduced in regions where $dT_w/dx \gg 1$ if convection is strong.

Instances of very high Pe^*, as shown in Fig. 7, indicate $\bar{T}$ matches qualitatively the profile of T_w. Asymptotic analysis of (48) for $\mathrm{Pe}^* \gg 1$ confirms this but is deferred until the following section within the context of rimming flows.

3.2.1. Effect of lateral conduction

In regions of large temperature gradients in the film lateral conduction, the terms $\alpha\partial^2 T/\partial x^2$ in (46) and $\alpha d^2\bar{T}/dx^2$ in (48) may become locally important. Physically this acts to smooth sharp changes in the temperature field and in numerical solutions it provides an important stabilising mechanism. This term is important around $x = \pm L$ where T_w changes rapidly but is negligible outside this region.

Inclusion of this term is illustrated in profiles of $\bar{T}$ obtained for both $\alpha = 0$ and $\alpha \neq 0$ in Fig. 8. In (a) (and shown in detail in (b)) the case $\alpha = 0$ illustrates a small numerical instability around the end of the heated section at $x = 1$. When lateral conduction is included ($\alpha \neq 0$), as illustrated in (c) and (d), this is smoothed. There is no significant difference outside this area.

4. Temperature profiles for rimming flow with steady-state constant film height

An important application is to investigate the thin film temperature field in a rimming flow of constant film height such as corresponding to thin high speed film flow. Inhomogeneity in the temperature profiles arises from a heated patch on the cylinder wall; the wall temperature outwith the patch is $T = 1$, the patch is at temperature $T = 1.5$. A Dirichlet temperature boundary condition at the film surface is imposed.

The mathematical formulation corresponds to solving the depth-averaged energy equation (48) and the two dimensional energy Eq. (46) with the independent variable x replaced by the cylindrical coordinate s and periodic conditions at $s = \pm\pi$ imposed on $\bar{T}$ and T respectively. The wall temperature profile (45) is restricted to the range $-\pi \leqslant s \leqslant \pi$. The case $k = 10$ with $L = 1$ is examined

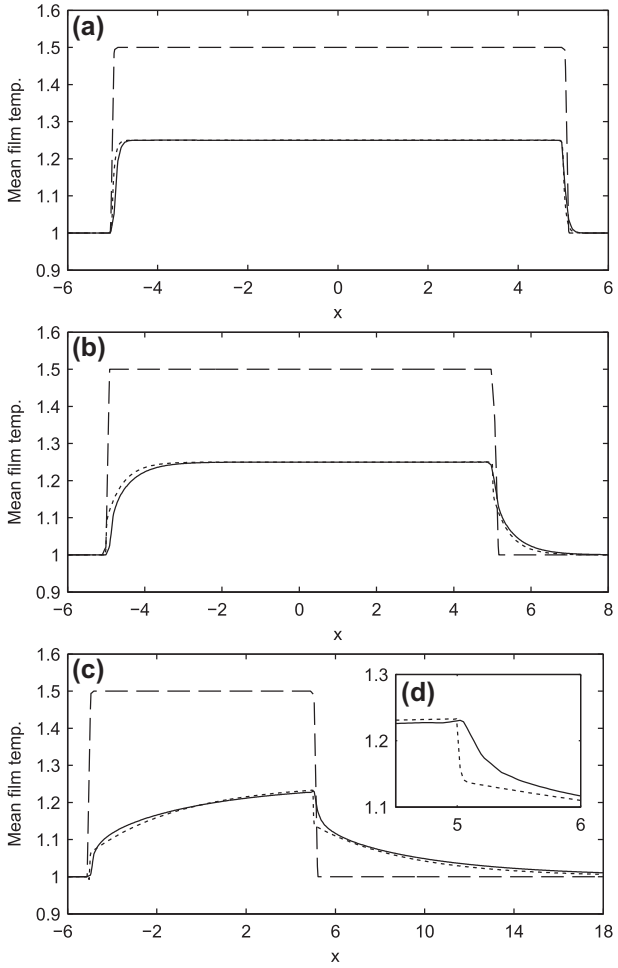

Fig. 5. Mean film temperature for the depth-averaged (·····) and 2D finite difference (—) methods. Wall temperature profile T_w indicated by (- - -). (a) $\mathrm{Pe}^* = 1$, (b) $\mathrm{Pe}^* = 10$ and (c) $\mathrm{Pe}^* = 100$. (d) shows the detail of $\bar{T}$ around $x = L$ for $\mathrm{Pe}^* = 100$. $T_a = 1,\ T_b = 1.5,\ \varepsilon = 0.1,\ L = 5,\ k = 100$.

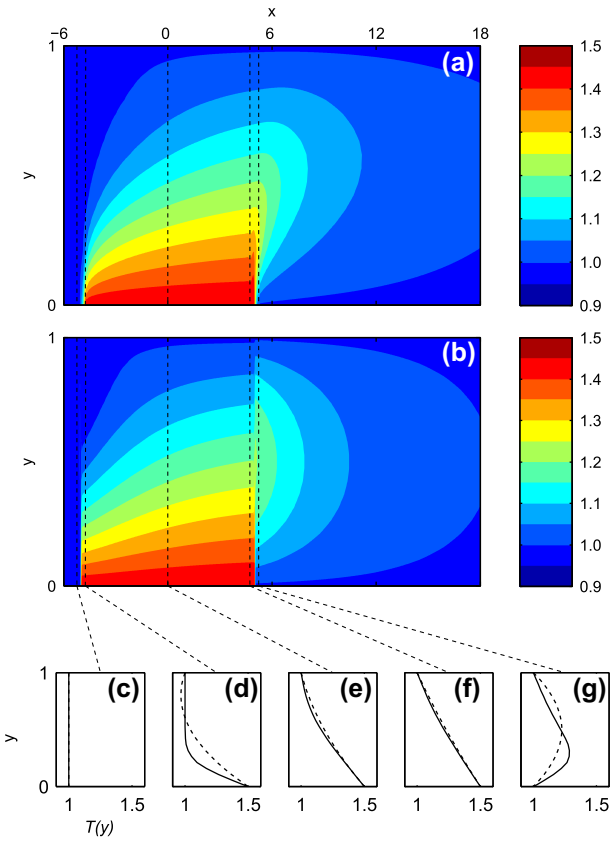

Fig. 6. Temperature fields for $\mathrm{Pe}^* = 100$ with $k = 100$ using (a) 2DFD and (b) DA solution methods. (c)–(g) show temperature profiles through the film at points indicated by connecting lines; 2DFD solution (—) and depth-averaged solution (- - -). Other parameters as in Fig. 5.

such that T_w returns to T_a with numerical accuracy within the s-domain. The numerical solver as described in Section 3.1 is extended to impose periodic conditions on T replacing the far-field conditions.

Mean film temperature profiles from the depth-averaged model (48) and 2DFD solution are plotted in Fig. 9 for $\mathrm{Pe}^* = 1, 10, 100$ and $10,000$. The case $\mathrm{Pe}^* = 10,000$ is selected to show the limiting behaviour of the model. At low Pe^* heat convection is sufficiently weak ((a) and (b)) that heat introduced to the film at the patch is quickly conducted back into the boundaries. As Pe^* increases (c) convection extends the heated region sufficiently to prevent the temperature returning to that of the unheated wall and $T > T_a$ everywhere.

In the limiting case of very high convection (Fig. 9(d)) the film temperature remains constant as conduction through the boundaries is relatively weak. The mean film temperature in this case matches the profile of T_w closely as can be verified by examining (48) asymptotically which, for $\mathrm{Pe}^* \gg 1$, gives $\mathrm{d}\bar{T}/\mathrm{d}s = (1/6)\mathrm{d}T_w/\mathrm{d}s$. Integrating and applying the piecewise value for T_w between the heated region (T_{wA}) and non-heated region (T_{wB}) gives the relation $\bar{T}_A - \bar{T}_B = (T_{wA} - T_{wB})/6$ for $\mathrm{Pe}^* \gg 1$. For the case in Fig. 9(d), numerical results give $\bar{T}_A - \bar{T}_B = -0.080$ and $(T_{wA} - T_{wB})/6 = -0.083$ which are in very good agreement although it is noted that the absolute value for $\bar{T}$ must be obtained by solving (48).

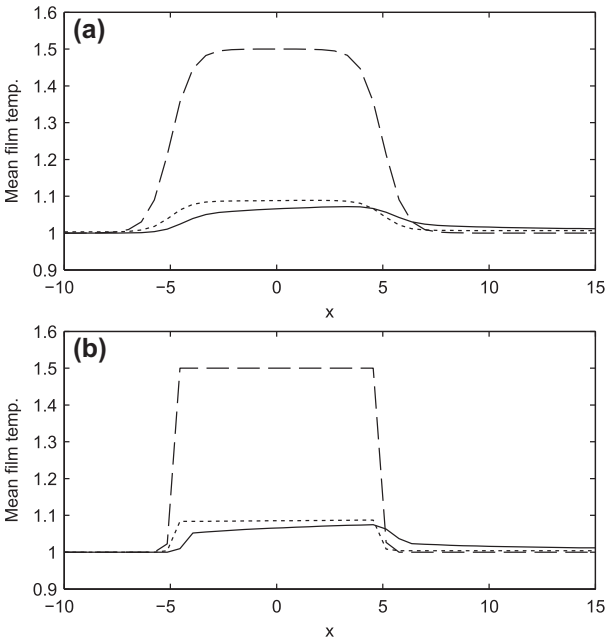

Fig. 7. The effects of strong convection for (a) a smooth wall temperature profile where $k = 1$ and (b) a stepped profile where $k = 10$. Solution of depth-averaged Eq. (48) (—) and solution of (46) using 2DFD (—). $\mathrm{Pe}^* = 10^4,\ T_a = 1,\ T_b = 1.5,\ \alpha = 0.01,\ L = 5$.

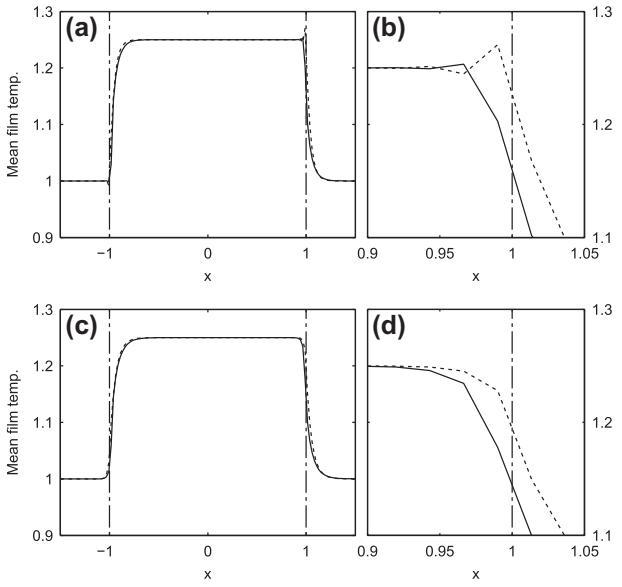

Fig. 8. Effect of lateral conduction on $\bar{T}$ calculated from 2DFD solution (—) and depth-averaged solution (· · · · · ·). In (a) $\alpha = 0$; (b) detail around $x = 1$; (c) $\alpha = 0.01$; (d) shows detail around $x = 1$. $T_a = 1,\ T_b = 1.5,\ \mathrm{Pe}^* = 1,\ L = 1$.

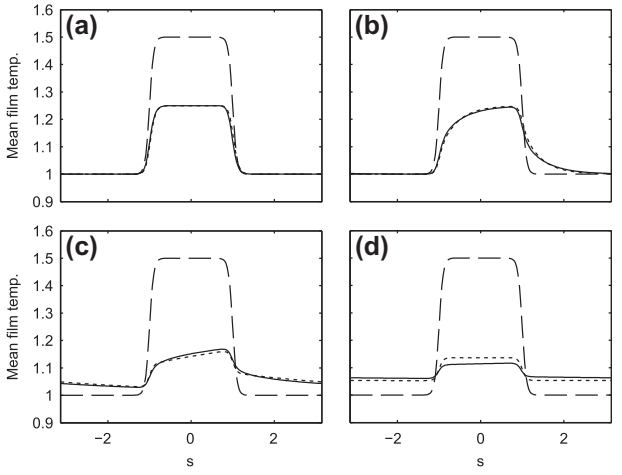

Fig. 9. Mean film temperature for uniform rimming flow of constant film height. (· · · · · ·) solution of depth-averaged formulation and (—) solution of the two-dimensional temperature field. Wall temperature profile (- - -). (a) $\mathrm{Pe}^* = 1$, (b) $\mathrm{Pe}^* = 10$, (c) $\mathrm{Pe}^* = 100$ and (d) $\mathrm{Pe}^* = 10,000$. $\varepsilon = 0.1,\ L = 1,\ k = 10,\ T_a = 1,\ T_b = 1.5$.

5. Temperature profile for a general rimming flow

The film profile and temperature field arising in a general rimming flow, determined by (35) from the competing effects of gravity and surface shear and modified by surface tension, inertial effects and gradients of hydrostatic pressure, is studied. The corresponding film temperature is determined from (33). In the remainder of the paper uniform air and wall temperatures, at $T_a = 0.5$ and $T_w = 1$ respectively, are taken and the Robin boundary condition (25) applied at the film surface.

The full system of Eqs. (33)–(35), are solved numerically to obtain $h,\ q$ and $\bar{T}$ as functions of s using a transient solver following that described in Section 3.1. A fully-implicit time stepping scheme with first-order forward-difference approximations for the time derivative was used. During solution the filling fraction of the solution was calculated at each time step and monitored to ensure constancy. Numerical solution were taken as converged to a steady-state solution if all residuals $r_i = \max[(f_i - f_{i-1})/f_i] < 10^{-5}$, where f_i corresponds to any of $h,\ q$ or $\bar{T}$ at the ith time-step.

5.1. Steady state film dynamics

For a steady-state solution the flux q is constant and depends on the filling fraction A[22] which in the context of this work is defined to $O(\varepsilon)$ as $\pi A = \varepsilon \int_{-\pi}^{\pi} h ds$. This, and the physical parameters (12), govern the solution types cited in Section 1. The temperature field in three types of rimming flow solution are investigated corresponding to a smooth solution, shock solution and pooling solution; characteristic flow profiles for these solutions types are shown illustrated in Fig. 10 and briefly described.

5.1.1. Smooth solutions

For $\lambda \sim O(1)$ (Fig. 10)(a)) and A small (0.02 in this study) the gravitational body forces in the film are insufficient to overcome the surface shear stress. The film will be smoothly distributed over the cylinder wall and the velocity field will be unidirectional. Typically the film will be thicker on the rising side of the cylinder as gravity acts against the surface shear and thinner on the falling side; the profile will satisfy $\partial h/\partial s \ll 1$.

5.1.2. Shock solutions

For $\lambda \sim O(1)$ (Fig. 10(b)) as A is increased (0.14 in this study) an accumulation of fluid forms on the rising side of the cylinder. Above a critical value of A this accumulation begins to form a recirculation region as the surface shear is unable to maintain the unidirectional flow. The film profile in this region is characterised by having a steep front where $\partial h/\partial s \gg 1$.

5.1.3. Pool solutions

For $\lambda > 1$ (Fig. 10(c)) as A is increased (0.2 in this study) the shock location will move downwards on the rising side of the cylinder to accommodate the excess fluid. Beyond a critical value of a pooling solution configuration exists in which the excess fluid is held in a recirculating pool in the bottom of the cylinder with a thin film of unidirectional flow covering the remainder of the wall.

An important feature of the depth-averaged approach is inclusion of inertia as a leading-order mechanism to provide transition between these solution types. Studies using lubrication theory for rimming flows [25] obtain a critical value of the filling fraction A_c, and a critical flux q_c, above which smooth solutions cannot be found. Solutions with larger A require excess fluid to be held in a discontinuous shock configuration. The inclusion of inertial effects allows a smooth solutions to exist when $q > q_c$. This permits a full range of solutions to be obtained beginning at the low-Re^* shock/pool solutions up to a smooth rimming flow with $q > q_c$.

The parameters governing the dynamics of the three solution types, chosen to ensure formation of either a smooth rimming

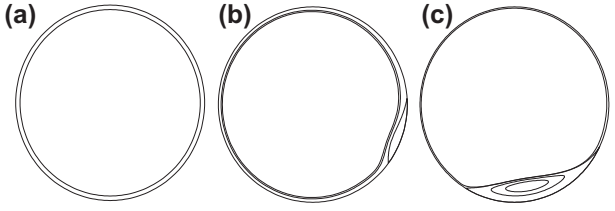

Fig. 10. Solution types for rimming flow. (a) smooth unidirectional flow, (b) shock solution, (c) pooling solution. The radial scale has been magnified ×25 in (b) to show the structure of the flow field. The surface shear stress acts to drive the film in the anticlockwise direction.

flow, a pool or a shock profile in the long-time evolution of the transient solver, are given in Table 1.

5.2. Temperature profiles in film solutions

Mean film temperature profiles are calculated for the smooth, shock and pool solutions and film temperature fields reconstructed. The effect of the strength of convection and inertia on these solutions is investigated by calculating for a range of values of Pe^* and Re^*. The model (33)–(35) is solved to obtain h, q and $\bar{T}$, the mean film quantities, and the two-dimensional temperature field $T(s,y)$ recovered from these using (36).

5.2.1. Smooth solutions

The temperature field in the smooth solution and the effect of the interface heat transfer coefficient is examined. Mean film temperature profiles with $Pe^* = 0.01$ for $B = 0.1$ and $B = 0.01$ are shown in Fig. 11(a). For $B = 0.01$ the mean film temperature is higher than for $B = 0.1$ since the interfacial heat flux is reduced by (25). Profiles of T through the film at the top of the cylinder ($s = \pm\pi$) shown in Fig. 11(b) confirm this. This was observed in [17] for locally-heated planar films where surface temperatures remained elevated downstream of the region of local heating for small surface Biot numbers.

Solutions show an independence from the value of Pe^*, and hence convection, and results for $Pe^* = 10$ are identical to those in Fig. 11. This is confirmed by the linear film temperature profiles in Fig. 11(b) and explained by (33) where convection depends on azimuthal gradients in the flow and boundary conditions which are zero in this case of a flat film.

5.2.2. Pool solutions

As an initial study the effect of convection on the temperature field of the pooling solution with $Re^* = 1$ is examined. In this and all remaining cases $B = 0.1$ is chosen; for $B = 0.01$ the mean film temperature is essentially uniform and shows little dependence on either the film height profile or strength of convection. Streamlines of this solution are illustrated in Fig. 12. The temperature field for a range of values of Pe^* are examined over which the solution exhibits distinct characteristics.

Table 1
Parameters governing dynamics of the non-isothermal rimming flow solutions, $\tau = 1$ and $\lambda = 1$.

Solution	ε	Re^*	Ca	A
Smooth	10^{-2}	1	10^{-1}	0.008
Pool	10^{-1}	$0.1 - 100$	10^{-1}	0.200
Shock	10^{-2}	$0.1 - 200$	10^{-3}	0.014

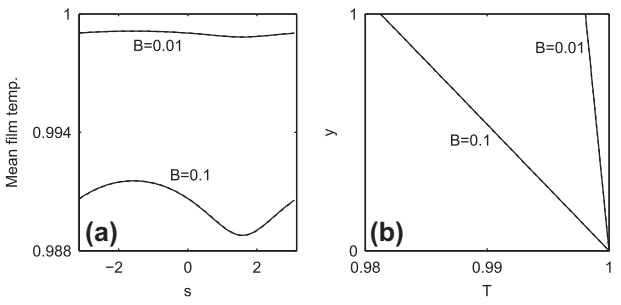

Fig. 11. Effect of B on smooth solution temperature field for $Pe^* = 0.01$. (a) mean film temperature and (b) temperature profiles through film depth at $s = \pm\pi$.

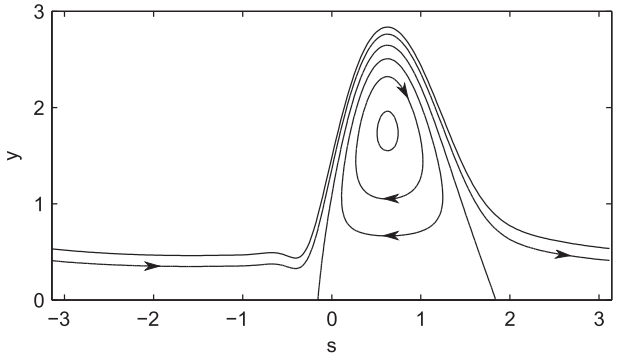

Fig. 12. Streamlines of the pool solution with $Re^* = 0.1$ showing the recirculation. Other parameters as given in Table 1.

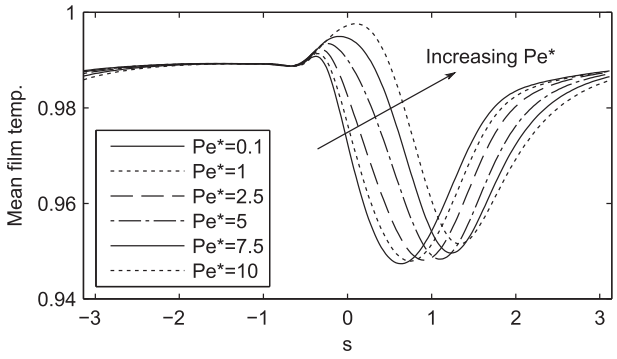

Fig. 13. Effect of convection on mean film temperature of pooling solution.

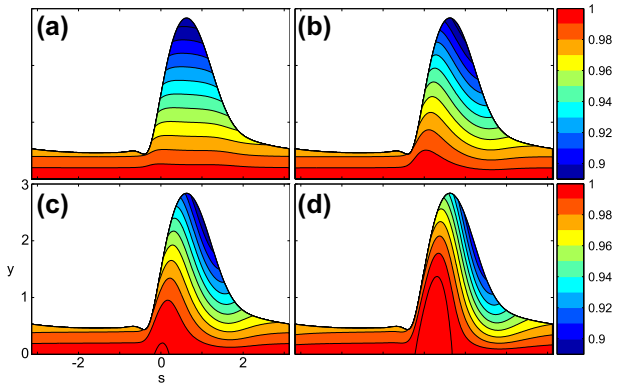

Fig. 14. Effect of convection on temperature distribution in a pool solution. Temperature contours for (a) $Pe^* = 0.1$, (b) $Pe^* = 1$, (c) $Pe^* = 5$ and (d) $Pe^* = 10$.

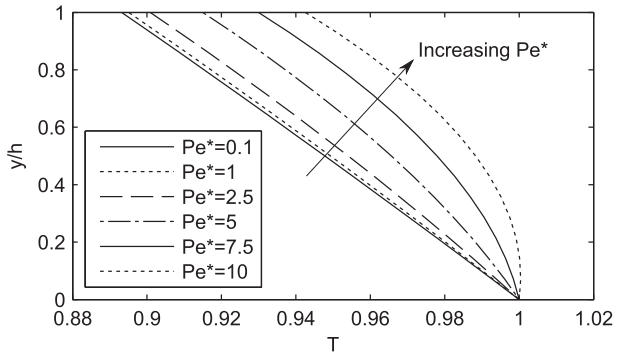

Fig. 15. Temperature distribution through the pool at the point of maximum depth for $Re^* = 0.1$.

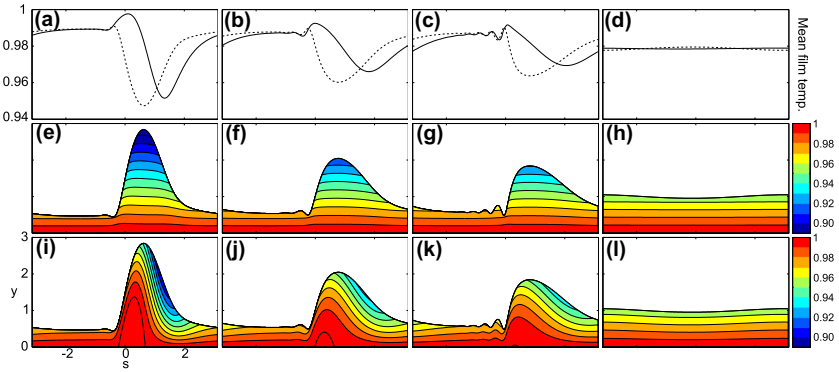

Fig. 16. Effect of Re^* on the film temperature in the pool solution. Panels (a)–(d) show mean temperature profiles with (· · · · · ·) indicating $Pe^* = 0.1$ and (—) $Pe^* = 10$. Panels (e)–(l) show reconstructed temperature fields. The first column of panels show $Re^* = 0.1$, second $Re^* = 5$, third $Re^* = 10$ and fourth $Re^* = 100$. The second row of panels have $Pe^* = 0.1$, the third $Pe^* = 10$.

Profiles of mean film temperature are shown in Fig. 13 and the corresponding temperature field in Fig. 14. The cooled region in the pool is driven downstream with increasing convection. There is an increase in mean temperature at the entrance to the pool as Pe^* is increased caused by the capillary waves. Outside of the recirculation the mean film temperature does not change significantly with Pe^*.

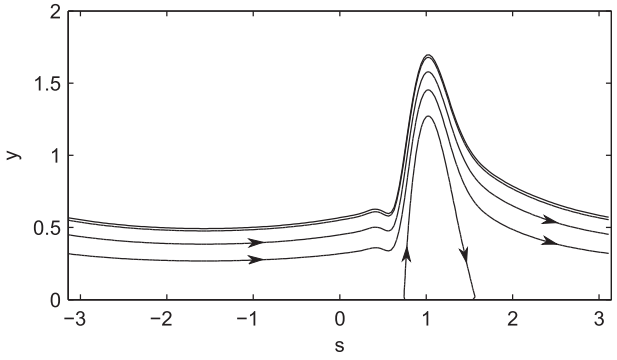

Fig. 17. Streamlines of the film flow for the shock solution $Re^* = 0.1$. Other parameters as given in Table 1.

Temperature contours in Fig. 14 show the recirculation strongly influences the temperature field. At low Pe^* (a) the film temperature is driven by cross-film conduction, is lowest furthest from the wall and shows no dependence on the velocity field. As Pe^* is increased (b) the recirculation moves the cooled region towards the wall. At the highest Pe^* the temperature is significantly raised in the pool ((c) and (d)).

Temperature profiles through the maximum depth of the film, shown in Fig. 15, confirm the transition between conduction- and convection-dominant flows and become increasingly nonlinear as Pe^* is increased.

As described, the depth-averaged model (33)–(35) can describe a range of film profiles from low-Re^* pooling through high-Re^* uniform flow. In this section the film temperature is examined across this range for a conduction-dominant ($Pe^* = 0.1$) and convection-dominant ($Pe^* = 10$) flow. Beginning at $Re^* = 0.1$ (recirculating pool), (33)–(35) are solved for $Re^* = 5, 10$ and 100 (uniform flow). The case $Re^* = 100$ lies outside the bounds given in (23) but with $h' \ll 1$ inertia is negligible and the solution remains valid.

Mean film temperatures are shown in Fig. 16(a)–(d), corresponding reconstructed temperature fields in (e)–(l). Low Re^* cases

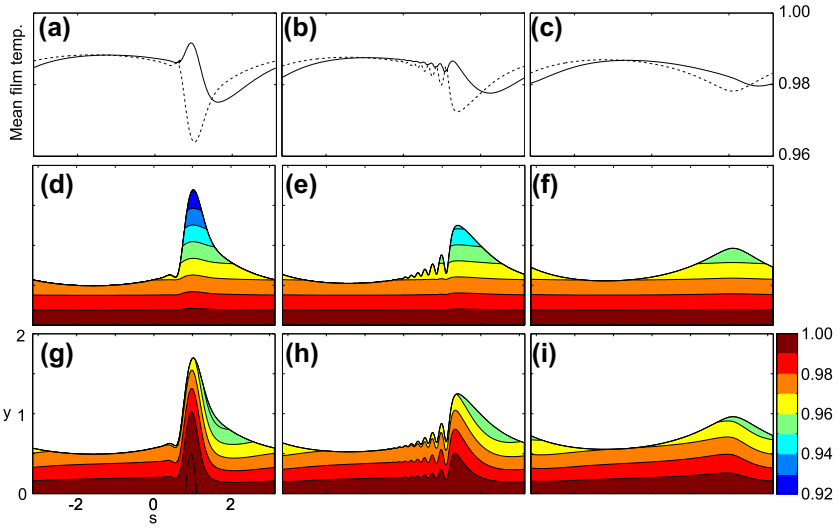

Fig. 18. Effect of Pe^* and Re^* on the film temperature for a shock solution. (a)–(c) show mean temperature profiles and (d)–(i) show film temperature fields. In (a), (d) and (g) $Re^* = 0.1$, in (b), (e) and (h) $Re^* = 10$ and in (c), (f) and (i) $Re^* = 20$. Mean temperature profiles are shown for $Pe^* = 0.01$with (· · · · · ·) and $Pe^* = 10$ with (—). In (d)–(f) $Pe^* = 0.01$, in (g)–(i) $Pe^* = 10$.

((a) and (b)) exhibit the conduction- and convection-dominant characteristics of a cooled and heated pool respectively. Increasing inertial effects flatten then film, the temperature becomes circumferentially uniform and independent of convection (d).

5.2.3. Shock solutions

The same analysis is repeated for a film profile containing a shock structure. Values of $Re^* = 0.1, 10$ and 20 characterise the transition between shock and uniform flow and $Pe^* = 0.01$ and 10 represent conduction- and convection-dominant flows. Streamlines of the flow field for $Re^* = 0.1$ are shown in Fig. 17. The mean and reconstructed film temperatures are illustrated in Fig. 18.

As in the pool, the shock is cooled (heated) in conduction-(convection-) dominant flows. As the film height profile becomes increasingly uniform with stronger inertia the film temperature at both $Pe^* = 0.01$ and $Pe^* = 10$ becomes circumferentially uniform. For cases of weak convection the mean temperature is observed to follow inversely the profile of the film height and this reversed when convective effects dominate.

6. Conclusions

A simplified approach to modelling the two-dimensional temperature distribution within a fluid film flow is established. This approach is applicable to film flows extending lubrication theory to films with moderate inertia and heat convection effects.

Modelling is based on assuming a quadratic dependency for temperature and velocity through the depth of the film. A spatially one-dimensional depth-averaged film temperature and velocity are first obtained and the corresponding two-dimensional fields reconstructed using the quadratic profiles. The effect on the film temperature field of increasing inertia and heat convection represents the major novel contribution of this work.

The robustness of the approach and numerical scheme was tested in the simplified case of a uniform flat film on a horizontal plate containing a heated patch. Results from the one-dimensional model are compared to those obtained from a numerical solution of the full two-dimensional film temperature field and an analytic solution.

The film temperature field from the one-dimensional depth-averaged model is in close agreement to the two-dimensional model particularly for low-Pe^* conduction-dominant flows. For convection-dominant flows (higher Pe^*) the depth-averaged solution was found to become inaccurate where sharp changes in boundary temperature existed. This is attributed to the limitations of a quadratic temperature profile which does not allow local temperature changes resulting from convection effects to be resolved without affecting the global temperature field. In cases where the boundary temperatures are smooth these inaccuracies are reduced and the depth-averaged model provides a very good estimation of the average temperature. In some cases reconstruction of the two-dimensional temperature field is limited by the quadratic profile assumption.

The depth-averaged model was used to investigate the temperature field for some characteristic rimming-flow solutions: smooth uniform flow, shock solution and pooling solution. The model predicted the heating of recirculation regions in the shock and pool solutions when the heat convection term was dominant. As inertial effects in the film increase and dynamically these recirculation gave way to a smooth uniform flow, these regions showed consequential cooling. In cases of weak convection the film temperature field had little dependence on the flow field.

Acknowledgements

The authors would like to thank Rolls-Royce plc for its financial and technical support and the UK Technology Strategy Board for its financial support of the SAMULET Program. The views expressed in this paper are those of the authors and not necessarily those of Rolls-Royce plc, Aerospace Group.

Appendix A. Coefficient functions for inertia and convection integrals

The dynamic coefficient functions in expressions (42) and (43) are

$$\begin{aligned} I^0 &= h^3\tau^2/120 + h\tau q/20 + 6q^2/5h, \\ I^1 &= -h^4\tau^2/240 - 3h^2\tau q/80 - 3q^2/40, \\ J^0 &= h^4\tau^2/160 + 3h^2\tau q/40 + 33q^2/40, \\ K_h^0 &= h\tau q/8 + 33q^2/40h + h^3\tau^2/160, \\ K_q^0 &= -h^2\tau/40 - q/2, \\ f^0 &= 3\tau/2 - 3q/h^2, \quad f^1 = -5h\tau/8 - 15q/4h \end{aligned} \tag{A.1}$$

and the thermal coefficients

$$\begin{aligned} M^0D = {} & \tau h^3 BT_a/30 - \tau h^3 BT_w/120 + \tau h^2\bar{T}/10 - \tau h^3 B\bar{T}/40 \\ & - \tau h^2 T_w/10 + qhBT_a/10 - 3qhBT_w/20 + 24q\bar{T}/5 \\ & + 21qBh\bar{T}/20 - 4qT_w/5, \end{aligned}$$

$$M^1D = (\tau h^2 + 6q)h(-4hBT_a + hBT_w - 12\bar{T} + 3Bh\bar{T} + 12T_w)/480,$$

$$\begin{aligned} W^0D = {} & h(6\tau h^3 BT_a - \tau h^3 BT_w + 36\tau h^2\bar{T} - 16\tau h^2 T_w + 36qhBT_a \\ & - 30qhBT_w + 792q\bar{T} + 144qBh\bar{T} - 192qT_w)/240, \end{aligned}$$

$$\begin{aligned} Z_h^0D = {} & \tau h^3 BT_a/40 - \tau h^3 BT_w/80 + 7\tau h^2\bar{T}/20 + \tau h^3 B\bar{T}/20 \\ & - \tau h^2 T_w/10 + 3qhBT_a/20 - qhBT_w/8 + 33q\bar{T}/10 + 3qBh\bar{T}/5 \\ & - 4qT_w/5, \end{aligned}$$

$$Z_q^0D = -h(4hBT_a - 3hBT_w + 80\bar{T} + 14Bh\bar{T} - 20T_w)/40,$$

$$Q^0Dh = 6hBT_a + 6hBT_w - 12\bar{T} - 12Bh\bar{T} + 12T_w,$$

$$Q^1D = hBT_w + 6T_w - hBT_a - 6\bar{T}.$$

References

[1] G. Seiden, P. Thomas, Complexity, segregation and pattern formation in rotating-drum flows, Rev. Mod. Phys. 83 (2011) 1323–1365, http://dx.doi.org/10.1103/RevModPhys.83.1323.

[2] E.D. Kay, S. Hibberd, H. Power, Inertial effects at moderate Reynolds number in thin-film rimming flows driven by surface shear, Phys. Fluids 25 (2013) 102108, http://dx.doi.org/10.1063/1.4825134.

[3] T.S. Strelkoff, One-dimensional equations of open-channel flow, J. Hydraul. Div. 95 (1969) 861–876.

[4] A.K. Rastogi, W. Rodi, Predictions of heat and mass transfer in open channels, J. Hydraul. Div. 104 (1978) 397–420.

[5] R.J. Gribben, R. Hunt, M. Abdelghaffar, G. Wilks, Evaluation of the approximate treatment of thin film flows, Applied Mathematical Modelling 14 (8) (1990) 420–426.

[6] B. Reisfeld, S.G. Bankoff, Non-isothermal flow of a liquid film on a horizontal cylinder, J. Fluid Mech. 236 (1992) 167–196, http://dx.doi.org/10.1017/S0022112092001381.

[7] G.A. Leslie, S.K. Wilson, B.R. Duffy, Non-isothermal flow of a thin film of fluid with temperature-dependent viscosity on a stationary horizontal cylinder, Phys. Fluids 23 (2011), http://dx.doi.org/10.1063/1.3593393.

[8] G.A. Leslie, S.K. Wilson, B.R. Duffy, Thermoviscous coating and rimming flow, Q. J. Appl. Math. 65 (4) (2012) 483–511, http://dx.doi.org/10.1093/qjmam/hbs013.

[9] S.W. Joo, S.H. Davis, S.G. Bankoff, Long-wave instabilities of heated falling films: two-dimensional theory of uniform layers, J. Fluid Mech. 230 (1991) 146–177, http://dx.doi.org/10.1017/S0022112091000733.

[10] T. Gambaryan-Roisman, Marangoni convection, evaporation and interface deformation in liquid films on heated substrates with non-uniform thermal conductivity, Int. J. Heat Mass Transfer 53 (2010) 390–402, http://dx.doi.org/10.1016/j.ijheatmasstransfer.2009.09.017.

[11] Z. Ding, T.N. Wong, Stability of a localized heated falling film with insoluble surfactants, Int. J. Heat Mass Transfer 67 (2013) 627–636, http://dx.doi.org/10.1016/j.ijheatmasstransfer.2013.07.098.
[12] J.M. Skotheim, U. Thiele, B. Scheid, On the instability of a falling film due to localized heating, J. Fluid Mech. 475 (2003) 1–19, http://dx.doi.org/10.1017/S0022112002001957.
[13] S. Miladinova, G.L. Slavtchev, J.-C. Legros, Long-wave instabilities of non-uniformly heated falling films, J. Fluid Mech. 453 (2002) 153–175, http://dx.doi.org/10.1017/S0022112001006814.
[14] A.M. Frank, 3D numerical simulation of regular structure formation in a locally heated falling film, Eur. J. Mech. B 22 (2003) 445–471, http://dx.doi.org/10.1016/S0997-7546(03)00056-6.
[15] E.Y. Gatapova, O.A. Kabov, I.V. Marchuk, Themocapillary deformation of a locally heated liquid film moving under the action of a gas flow, Tech. Phys. Lett. 30 (5) (2004) 418–421, http://dx.doi.org/10.1134/1.1760873.
[16] A.M. Frank, O.A. Kabov, Themocapillary structure formation in a falling film: experiment and calculation, Phys. Fluids 18 (2006) 032107-1–032107-10, http://dx.doi.org/10.1063/1.2187949.
[17] E.Y. Gatapova, O.A. Kabov, Shear-driven flows of locally heated liquid films, Int. J. Heat Mass Transfer 51 (2008) 4797–4810, http://dx.doi.org/10.1016/j.ijheatmasstransfer.2008.02.038.
[18] S. Kalliadasis, A. Kiyashko, E.A. Demekhin, Marangoni instability of a thin liquid film heated from below by a local heat source, J. Fluid Mech. 475 (2003) 377–408, http://dx.doi.org/10.1017/S0022112002003014.
[19] A.A. Nicol, Z.L. Aidoun, R.J. Gribben, G. Wilks, Heat transfer in the presence of condensate drainage, International Journal of Multiphase Flow 14 (3) (1988) 349–359.
[20] A. Costa, G. Macedonio, Numerical simulation of lava flows based on depth-averaged equations, Geophys. Res. Lett. 32 (2005), http://dx.doi.org/10.1029/2004GL021817.
[21] G.W. Recktenwald, P. Butler, Depth-averaged modeling of convective heat transfer from printed circuit boards, in: ASME Winter Annual Meeting, American Society of Mechanical Engineers, Atlanta, GA, 1991 (ASME Paper No. 91-WA-EEP-36).
[22] J. Ashmore, A. Hosoi, H. Stone, The effect of surface tension on rimming flows in a partially filled rotating cylinder, J. Fluid Mech. 479 (2003) 65–98, http://dx.doi.org/10.1017/S0022112002003312.
[23] A. Acrivos, B. Jin, Rimming flows within a rotating horizontal cylinder: asymptotic analysis of the thin-film lubrication equations and stability of their solutions, J. Eng. Math. 50 (2004) 99–120, http://dx.doi.org/10.1007/s10665-004-1772-7.
[24] L.T. Nguyen, V. Balakotaiah, Modeling and experimental studies of wave evolution on free falling viscous films, Phys. Fluids 12 (9) (2000) 2236–2256, http://dx.doi.org/10.1063/1.1287612.
[25] M. Villegas-Diaz, H. Power, D. Riley, Analytical and numerical studies of the stability of thin-film rimming flow subject to surface shear, J. Fluid Mech. 541 (2005) 317–344, http://dx.doi.org/10.1017/S0022112005006142.